ORIGINAL RESEARCH ARTICLE

Thermal Stability and Mechanical Properties of Cu-Nb Nanocomposite Thin Films

Y.G. Li 🄳, H. Chen, Y.C. Huang, and W.Y. Liu

Nanostructured Cu-Nb thin films with composition ranging from $Cu_{72}Nb_{28}$ to $Cu_{62}Nb_{38}$ were prepared by hybrid modulated pulsed power magnetron sputtering and pulsed dc magnetron sputtering to study the thermal stability and mechanical properties. Through a vacuum annealing treatment from 200 to 400 °C, the structure and mechanical properties of $Cu_{69}Nb_{31}$ thin films are insensitive to the thermal changes, despite Cu-Nb are generally thermal unstable in kinetic Monte Carlo modeling with its initial decomposition temperature of about 200 °C. The hardness and modulus of $Cu_{69}Nb_{31}$ films showed a slight decrease from 7.2 to 6.6 GPa and 168.4 to 165.3 GPa pre and post annealing, and the films were believed to be thermal insensitive over 400 °C. The thermal stability of Cu-Nb nanocomposite thin films is enhanced by highly dispersed Nb-rich nanoprecipitates embedded in a Cu-rich phase, and the multiple interfaces brought by Nb-rich nanoprecipitates and Cu-rich phase reinforced the solute drag effect and Zener pinning should be responsible for the enhanced thermal stability of Cu-Nb nanocomposite thin films.

1. Introduction

Nanostructured Cu-Nb thin films were proved to be a promising radiation tolerant material for nuclear applications (Ref 1-3). The capacity of radiation tolerance relied on the thermal stability of their nanostructure. However, nanostructured thin film, nanomultilayer or nanocomposite, still encounter thermal stability problem. For nanomultilayer thin films under high temperature, the interface tension between the layers led to form the thermal grooving causing film layer delamination (Ref 4). While for nanocomposite films under high temperature, the phase segregation and grain growth cannot be easily avoided owing to the thermal diffusion (Ref 5). Meanwhile, thermal spikes and atom displacements brought by the radiation process also sabotaged the nanostructure stability of the thin films (Ref 6, 7).

Despite, the encountered thermal stability problem of nanostructured thin film, tailoring a grain to nanoscale was still an effective way for obtaining thermal stable structure. Lu et al. (Ref 8) discovered that the stability of the copper

nanograins increased with the drop in the copper grain size when the copper grain size was tuned below 70 nm. The thermal stability relied on the energy drop of grain boundaries as well as the prohibition of the full dislocation movement turning to the activation of partial dislocation. For the binary alloys, the composition of the nanocrystal alloy was also an important influencing factor. Darling et al. (Ref 9) found that the addition of Zr into Fe helped to stabilize Fe nanograin in Fe-Zr alloys. Adding Zr into Fe nanoalloys to 4 at.% were reported to stabilize Fe grains of about 50 nm over 900 °C. The thermal stability of those nanograin alloys can be thermodynamically designed by using the mixing enthalpy and segregation enthalpy. Murdoch and Schuh (Ref 5) established a criteria for designing thermal stable binary alloy systems, where the segregation enthalpy ΔH_{seg} should be bigger than $c(\Delta H_{mix})^a$ in which ΔH_{mix} was mixing enthalpy. Chookajorn et al. (Ref 10) have successively predicted and prepared W-20Ti immiscible alloys with nanostructure stable over 1000 °C. Immiscible Cu-10 at.%Ta nanocrystalline alloys were also found to be stable at 600 °C before and after creep with the size Cu and Ta nanograin of about 1-5 nm and 20-100 nm. The reason for the stability of nanograins should be maintained by the coherent dispersion of the nanoclusters, and these nanoclusters pinned the grain boundaries (Zener pinning) preventing grain from coarsening (Ref 11).

Cu-Nb binary system is a typical immiscible material with its mixing enthalpy positive in crystallization state, while the mixing enthalpy can turn to be negative in amorphous state by sputtering (Ref 12). Puthucode et al. (Ref 13) investigated magnetron co-sputtered $Cu_{55}Nb_{45}$ films annealed at 200 to 400 °C for detailed crystallization observation of the multiple stages. The fcc Cu-rich phases were first segregated from the amorphous matrix forming fcc Cu-rich nanocrystals, and the remaining amorphous matrix partially transformed to a bcc phase encompassing the existing fcc Cu-rich nanocrystals during growth with the others further decomposed to fcc Cu nanocrystals. Zhang et al. (Ref 14) studied the thermal stability

of $Cu_{90}Nb_{10}$ alloy thin films and found that Nb precipitated rapidly with sharp slope at 400 °C. Cu-Nb thin films prepared by far from equilibrium process can form both miscible and immiscible alloys, the film composition and microstructure were much more complex than traditional nanocrystal alloys. Meanwhile, the ion bombardment was also an important factor for controlling the crystallinity of the Cu-Nb thin films (Ref 15, 16). Therefore, it is possible to tailor the mixing enthalpy of Cu-Nb thin films as well as crystallinity of Cu-rich phase by controlling the ion bombardment effect to study the thermal stability of a nanostructured thin film.

In this work, Cu-Nb thin films were deposited by a high ionized magnetron sputtering technique, called modulated pulsed power magnetron sputtering (MPPMS) (Ref 17), to control the ion bombardment effect in the film deposition process. The ionized degree of the plasma was tuned to deposit a Cu-Nb thin films with varied composition and structure, and substantial annealing was done to learn the stability of the microstructure with mechanical properties being compared.

2. Experimental Details

All Cu/Nb thin films were deposited by co-sputtering process of Cu (99.999% purity) and Nb (99.95% purity) targets in a closed field unbalanced magnetron sputtering system. A detailed description of the deposition device was reported previously (Ref 18). Cu and Nb targets with the size of 440 mm × 140 mm × 8 mm were installed oppositely with each other with a distance of about 525 mm. Cu target was driven by AE Pinnacle Plus in a fixed power mode of 1 kW with a frequency of 100 kHz. Niobium plate was powered at a manual mode with macropulse frequency of 50 Hz, generated through a Zpulser AXIS™ with a charging voltage of 400 V. The background pressure was vacuumed superior to 4.5×10^{-4} Pa. The argon, 99.99% purity, was introduced into the deposition chamber, whose pressure and mass flow rate were kept at 0.3 Pa and 80 sccm. The substrate holder was paralleled to the target surface, and the mean substrate to target distance of Nb and Cu was kept constant at 125 mm and 400 mm, respectively. The substrate self-rotates in a speed around 4.6 s/r. All samples with thickness of about 2 μm were applied with a bias of -50 V powered by Zpulser Vesta™. AISI 304 stainless steel was used as substrates which were ultrasonically cleaned in alcohol and acetone for at least 15 minutes, respectively, before mounted into the deposition chamber. No additional heat was applied to the substrate, and the T_s/T_m in the growth process is less than 0.1. The discharge waveform of MPPMS was recorded by Tektronix TDS2014C oscilloscope, and each discharge parameters were an average of

ten recorded data which were peak voltage V_p, peak current I_p, peak power P_p and average power P_a as listed in Table 1.

Film annealing process was performed in a vacuum chamber with a background pressure superior to 2.5×10^{-4} Pa. Before heating the samples, argon was introduced in the chamber with a pressure of 0.5 Pa to protect the samples from being oxidized. The samples were heated under 200 °C, 300 °C and 400 °C for 3 h in a heating rate of 5 °C/min, then cooling for 2 h before taking out of the chamber with argon protected in the whole process. Phase composition and microstructure of the films were characterized by using a Shimadzu LabX XRD-6000 diffractometer (XRD), Shimadzu EPMA-1600 electron probe microstructure analysis (EPMA) and JEOL JEM-F200 high-resolution transmission electron microscope (HRTEM). The TEM cross-sectional samples for HRTEM observation were fabricated by Helios G4 UX focused ion beam (FIB). The hardness (H) and elastic modulus (E) of the films were measured by MTS Nanoindenter XP™ equipped with a Berkovich diamond indenter. The indentation depth was selected below 10% of the film thickness to minimize the substrate effect. For each sample, at least nine effective measurements separated by a distance of 200 μm were made to obtain the statistical results.

3. Results and discussion

Figure 1 shows the XRD patterns of Cu-Nb thin films. Fig. 1(a) was for the as-deposited Cu-Nb thin films under a varied micropulse switch-on time with film composition varied from $Cu_{72}Nb_{28}$ to $Cu_{62}Nb_{38}$ measured by EPMA. For all Cu-Nb films, there was a diffraction peak located between Cu(111) and Nb(110) diffraction peak, the new peak can be labeled as Cu-rich phase owing to the incorporation of Nb atoms into Cu matrix (Ref 13, 19). Increasing the micropulse switch-on time from 7 to 11 μs, the intensity of Cu(111) and Nb(110) diffraction peaks gradually increased with the peak intensity of Cu-rich phase decrease. Banerjee et al. (Ref 20) reported that Cu-Nb thin films with Nb composition ranging from 30 to 70 at.% tended to show a typical amorphous-like feather. However, the crystallinity of Cu-Nb thin films lied not only on the composition but also momentum transfer per atom in the deposition process (Ref 21). Note that higher micropulse switch-on time corresponded with the high discharge current indicating the promotion of plasma density and momentum transfer per atom. As showed in Fig. 1(a), the $Cu_{69}Nb_{31}$ thin films were with vague Nb(110) diffraction peaks indicating the initiation of the Nb segregation, and the segregation is promoted by the increase in discharge current. As for the peak shift, one possible reason is the influence of residual stress variation. Since the deposition of different Cu-Nb thin films

Table 1 MPPMS discharge parameters for depositing Cu-Nb thin films

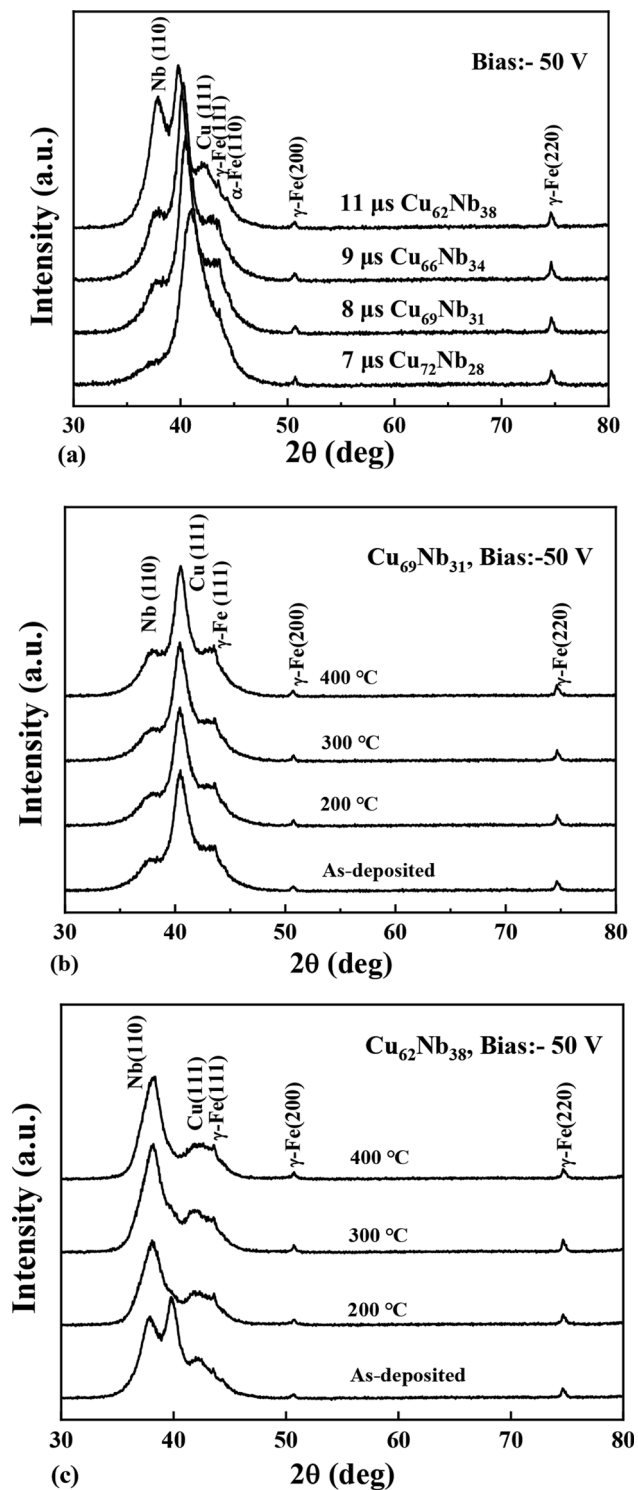| No	Charging voltage, V	Deposition time, s	Macropulse frequency, Hz	Strong ionization region τ_{off}/τ_{on}, μs	Argon flow, sccm	Bias, V	V_p, V	I_p, A	P_p, kW	P_a, kW
1	400	7000	50	10/7	80	-50	405.9	90.8	36.9	1.0
2	400	6000	50	10/8	80	-50	416.8	115.6	49.3	1.4
3	400	5500	50	10/9	80	-50	423.7	150.5	63.4	1.8
4	400	5000	50	10/11	80	-50	449.2	187.2	84.2	2.4

Fig. 1 XRD patterns of Cu-Nb thin films: (a) as-deposited Cu-Nb thin films; (b) $Cu_{69}Nb_{31}$ thin films before and after annealing process; (c) $Cu_{62}Nb_{38}$ thin films before and after annealing process.

was through the modulation of discharge current, and high discharge current will enhance the ion bombardment effect in turn influencing the residual stress.

In the annealing process, $Cu_{69}Nb_{31}$ and $Cu_{62}Nb_{38}$ were heated to 200, 300, and 400 °C to study the stability of the thin films. Fig. 1(b) and (c) shows the XRD patterns of $Cu_{69}Nb_{31}$ and $Cu_{62}Nb_{38}$ films after annealing process. For $Cu_{69}Nb_{31}$ films

after annealing process, the diffraction peaks of Nb(110) and Cu-rich(111) were almost stable in the whole process, and this implied the grain size for both Nb and Cu-rich phases was insensitive to temperature in this case. While for $Cu_{62}Nb_{38}$ films, the Cu-rich(111) phase quickly disappeared even at 200 °C. The increase in annealing temperature for $Cu_{62}Nb_{38}$ films resulted in the promotion of Nb(110) peak intensity with the broadened Cu(111) diffraction peak.

Figure 2 showed the calculation results of sputtered ion energy, mixing enthalpy and the vacancy recombination behavior of Cu-Nb thin films. To give a much clearer demonstration, TRIM and SIMTRA were used to calculate the sputtering and transportation behavior as showed in Fig. 2(a) (Ref 22, 23). The calculated ion energy on film surface with varied target-substrate distance suggested that the Nb sputtering species should show relatively higher energy. Since the substrate distance of Nb target was 125 mm lower than the Cu target, the arriving Nb ions on the film surface was higher endowing the surface movement for low migration Nb atoms. However, the as-deposited coatings with high niobium content were reported to be amorphous state (Ref 24, 25). The difference here should be considered to originate from the employment of MPPMS. In a MPPMS deposition process, the metal target sputtered a larger fraction of metal ions in contrast with conventional magnetron sputtering, high ionized plasma assisted the crystallization process of Cu-Nb thin films (Ref 26). Thereafter, higher MPPMS peak power promoted the crystallization of the coatings. The results gave the explanation of continuous precipitation of Nb grains as showed in Fig. 1. Meanwhile, higher ionized flux should also lead to a considerable interface mixing which in turn gave an unclear grain boundary (Ref 27).

Figure 2(b) shows the mixing enthalpy of Cu-Nb alloys calculated by using Miedema method (Ref 28, 29). It was found that the maximum mixing enthalpy was near stoichiometric ratio, and the ideal mixing enthalpy of Cu-Nb alloy should show an increase as the film composition varied from $Cu_{72}Nb_{28}$ to $Cu_{62}Nb_{38}$. However, the precipitated Nb in as-deposited Cu-Nb thin films suggested the mixing enthalpy should be negative. The thermal stability of $Cu_{69}Nb_{31}$ was prior to $Cu_{62}Nb_{38}$ thin films indicating the stability of Cu-Nb thin films not only relied on the mixing enthalpy. Vacancy and vacancy cluster recombination behaviors with Cu/Nb interface as a function of temperature modeled by using Kinetic Monte Carlo method are illustrated in Fig. 2(c) (Ref 30). The calculation detailed information was in the supplemental material. Vacancy and two vacancy clusters are shorted for V1 and V2, while interstitial atom and two interstitial atoms are shorted for I1 and I2. As the temperature increases, the vacancy movement is far more active for Cu with its saturation reaction temperature of about 200 °C, while the vacancies in Nb just begin to react at the about 200 °C. The interface absorbs vacancies in Cu more quickly both for V1 and V2. This indicates the stability of the Cu-Nb thin film should reply on the existence of Nb nanoparticles and Cu-riched phase. Clear Cu-Nb interface helped to promote the thermal diffusion in Cu-Nb thin films.

Further cross-sectional HRTEM observations for both as-deposited and annealing $Cu_{69}Nb_{31}$ thin films are illustrated in Fig. 3 and 4. Figure 3 was for the as-deposited samples, while Fig. 4 was for the samples after a 400-°C vacuum annealing treatment. The SEAD suggested that Cu-rich phase in Cu-Nb thin film before annealing mainly exhibited a face-centered cubic structure. For as-deposited $Cu_{69}Nb_{31}$ films and films
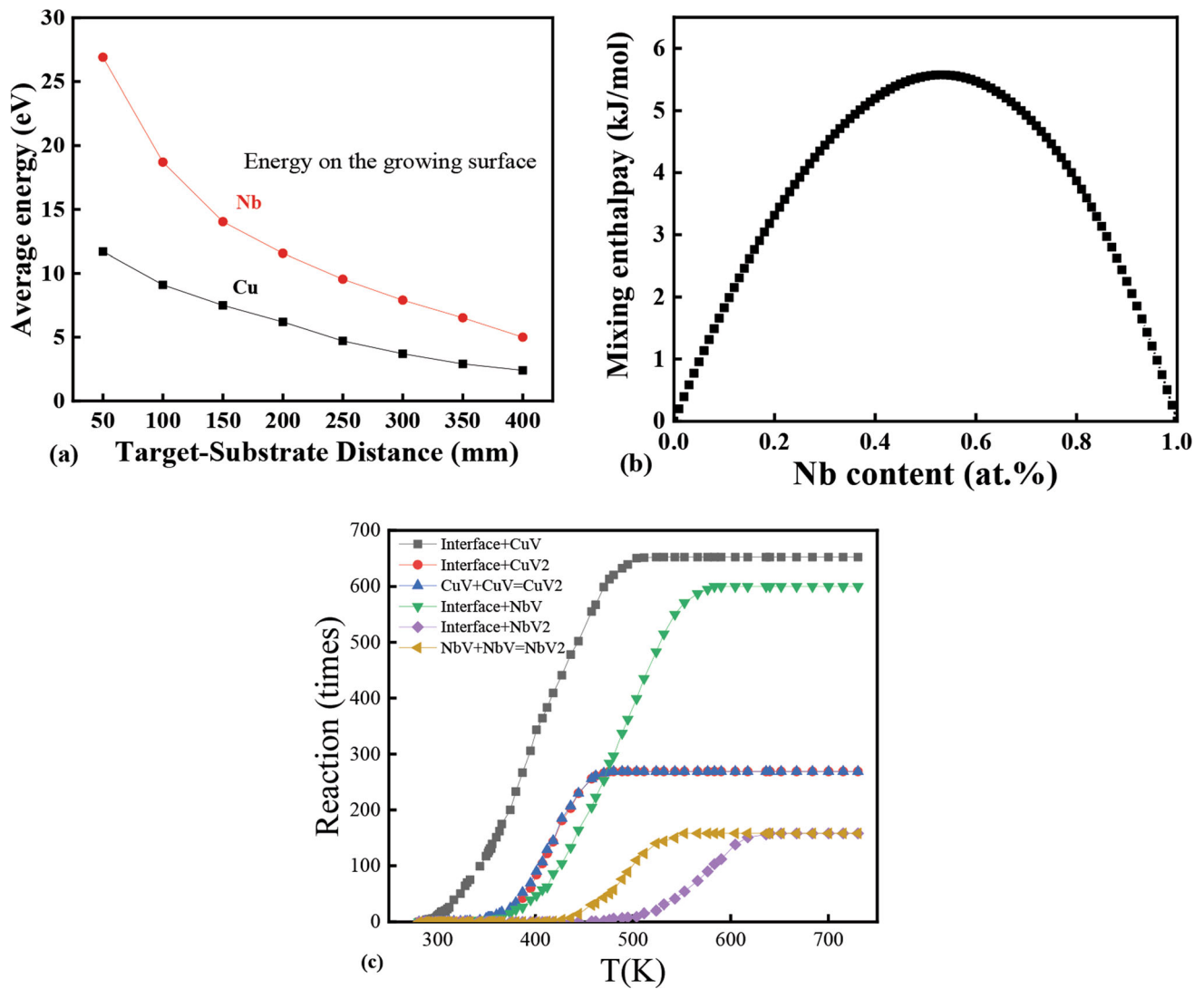
Fig. 2 Calculation results of sputtering energy, mixing enthalpy and kinetic Monte Carlo modeling results of Cu-Nb thin films: (a) input ion energy calculated by TRIM and SIMTRA; (b) mixing enthalpy of Cu-Nb alloys calculated by using Miedema method; (c) interstitial atoms and vacancy movement behaviors with Cu/Nb as a function of temperature.

being annealed, small Nb-rich precipitated particles could be observed both on grain boundaries and in Cu-rich phase, while the sizes of precipitated grains were relatively stable. The results confirmed the observation that grain sizes in $Cu_{69}Nb_{31}$ thin films were insensitive to temperature as showed in Fig. 1 after being annealed at 400 °C. Owing to the vacancy formation energy difference between copper and niobium, the vacancy concentration in copper is at least two orders of magnitude higher than that of niobium at the same temperature based on estimation through $N_v = N \exp\left(-\frac{Q_v}{kT}\right)$. The mobility of the copper atoms was much faster than niobium atoms as indicated in Fig. 2(c). Combined with analysis in Figs. 1, 3 and 4, the Cu-Nb thin films showed a typical nanocomposite structure with Nb-rich grains embedded into Cu-rich phases. The pining effect should lie on the gain size of Nb grains owing to the general grain boundary precipitation (Ref 19).

The results also showed an insight into the thermal stability of nc-TiN/a-Si$_3$N$_4$ type nanocomposite. Referring to the thermal behavior of Cu-Nb nanocomposite films, the limiting issues for nc-TiN/a-Si$_3$N$_4$ type nanocomposite with high thermal stability should be the amorphous phase since the amorphous phase can be crystalized with negative mixing entropy (Ref 31, 32). For high thermal stable nc-TiN/a-Si$_3$N$_4$ type nanocomposite, pseudocrystallization of amorphous Si$_3$N$_4$ on TiN phases should be preferred.

Figure 5 shows the hardness and modulus of Cu-Nb films before and after annealing. As the increase in micropulse on time, the hardness and modulus increased from 6.9 to 8.0 GPa, and 164.7 to 178.7 GPa illustrated in Fig. 5a. The slight increase in the hardness and modulus should be caused by consistent addition of the Nb content in the Cu-Nb films following the basic trend of rule of mixture values. Fig. 5(b) and (c) shows the hardness and modulus of $Cu_{69}Nb_{31}$ and $Cu_{62}Nb_{38}$ films as a function of annealing temperature. The hardness and modulus were quite stable after annealing. The hardness and modulus of $Cu_{69}Nb_{31}$ films showed a slight decrease from 7.2 to 6.6 GPa and 168.4 to 165.3 GPa, while the hardness and modulus of $Cu_{62}Nb_{38}$ films were around 8.0 and 176.0 GPa, respectively. The hardness and modulus were relatively stable after annealing indicating the decomposition of
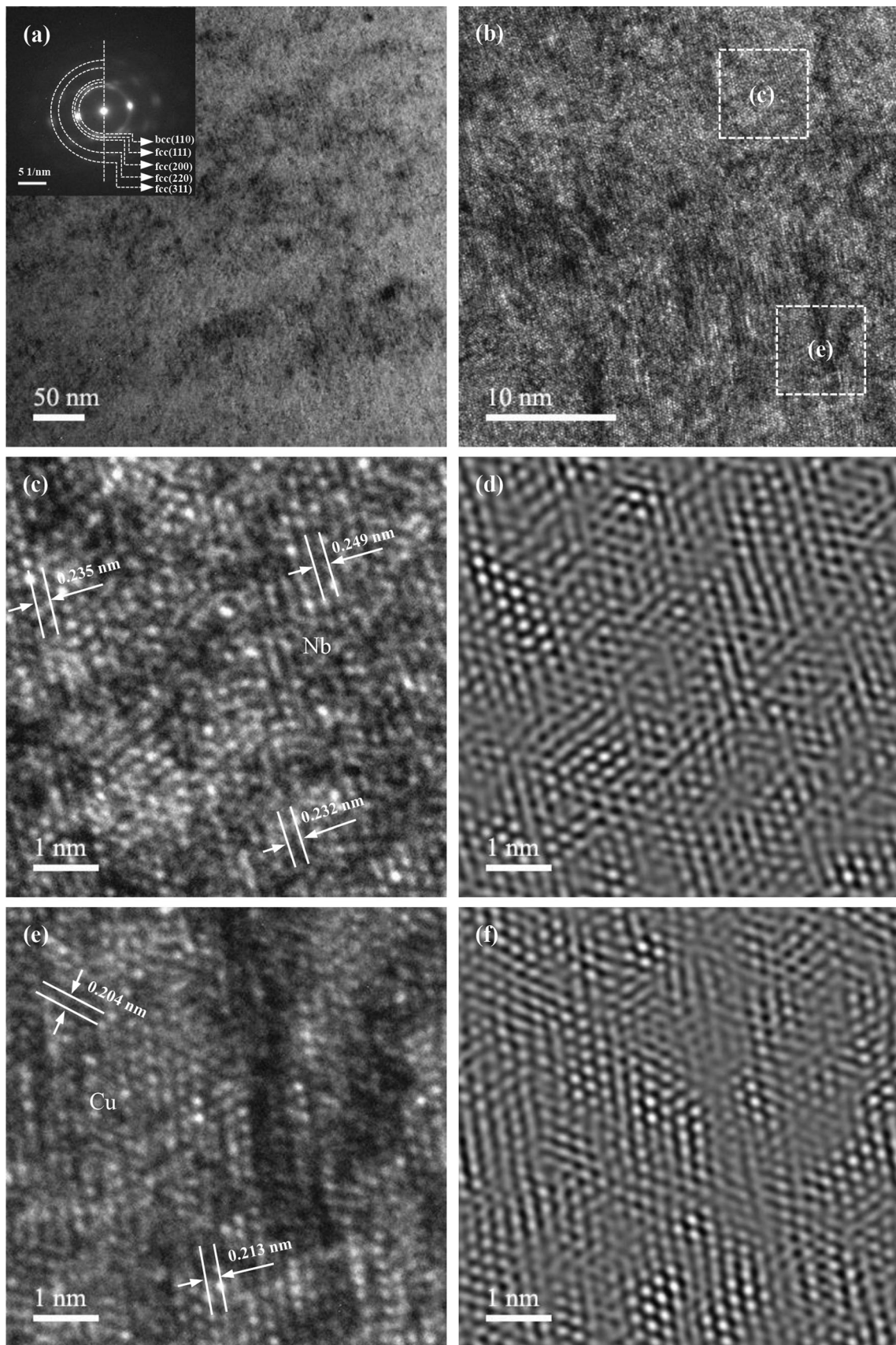
Fig. 3 Cross-sectional HRTEM and SAED images of as-deposited $Cu_{69}Nb_{31}$ thin films. (a) Low magnification TEM images and SAED patterns of Cu-Nb thin films. (b) HRTEM images. (c) Enlargement of images near a Nb precipitate. (d) Inverse fast Fourier-transform images of (c) highlighting the dislocations near the precipitate. (e) Enlargement of images near a Cu-rich phase. (f) Inverse fast Fourier-transforming images of (e).
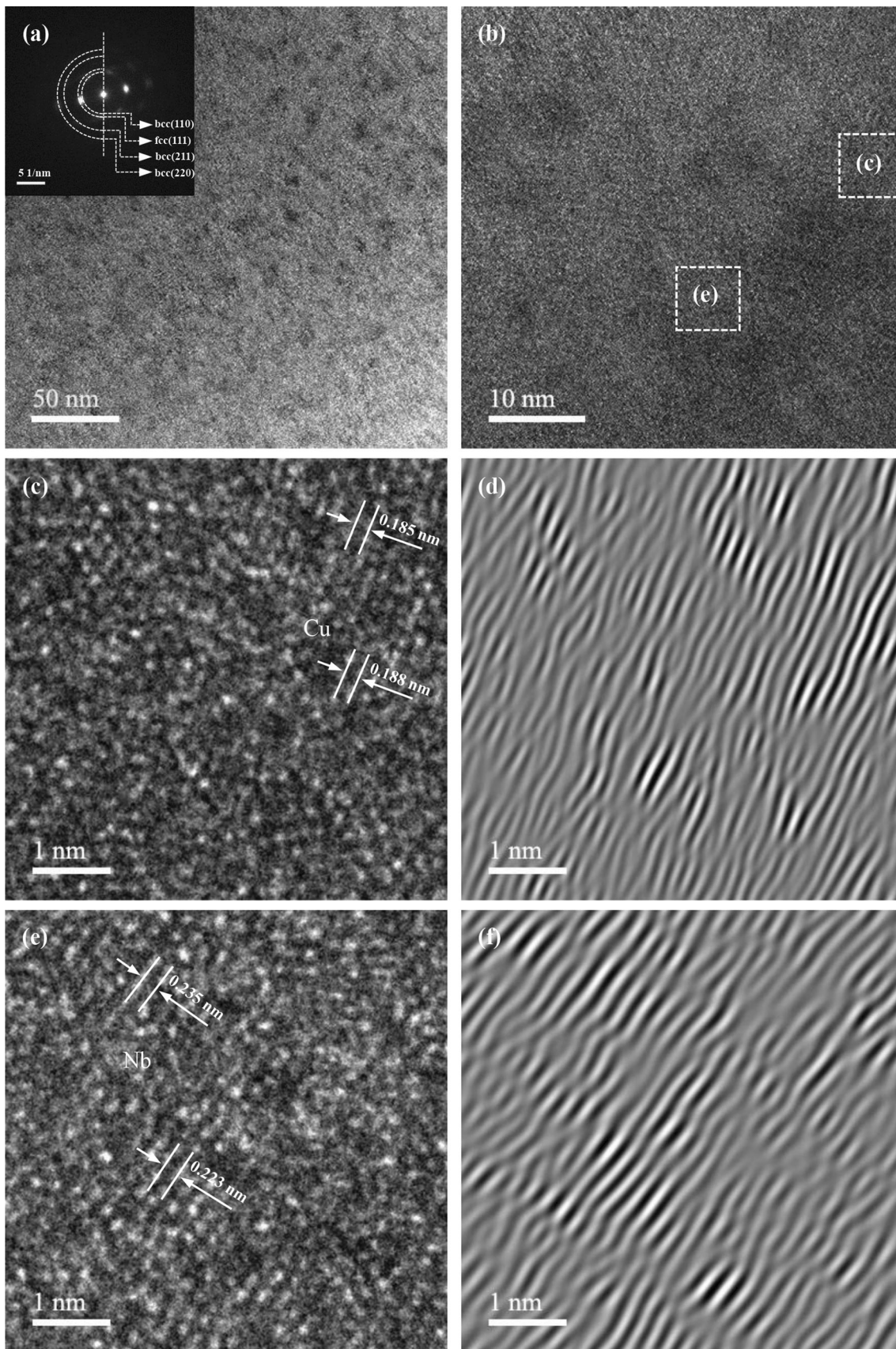
Fig. 4 Cross-sectional HRTEM and SAED images of $Cu_{69}Nb_{31}$ thin films after a 400-°C annealing process. (a) Low magnification TEM images and SAED patterns of Cu-Nb thin films. (b) HRTEM images. (c) Enlargement of images near a Cu-rich phase. (d) Inverse fast Fourier-transform images of (c) highlighting the dislocations near the Cu-rich phase. (e) Enlargement of images near a Nb precipitate. (f) Inverse fast Fourier-transforming images of (e).
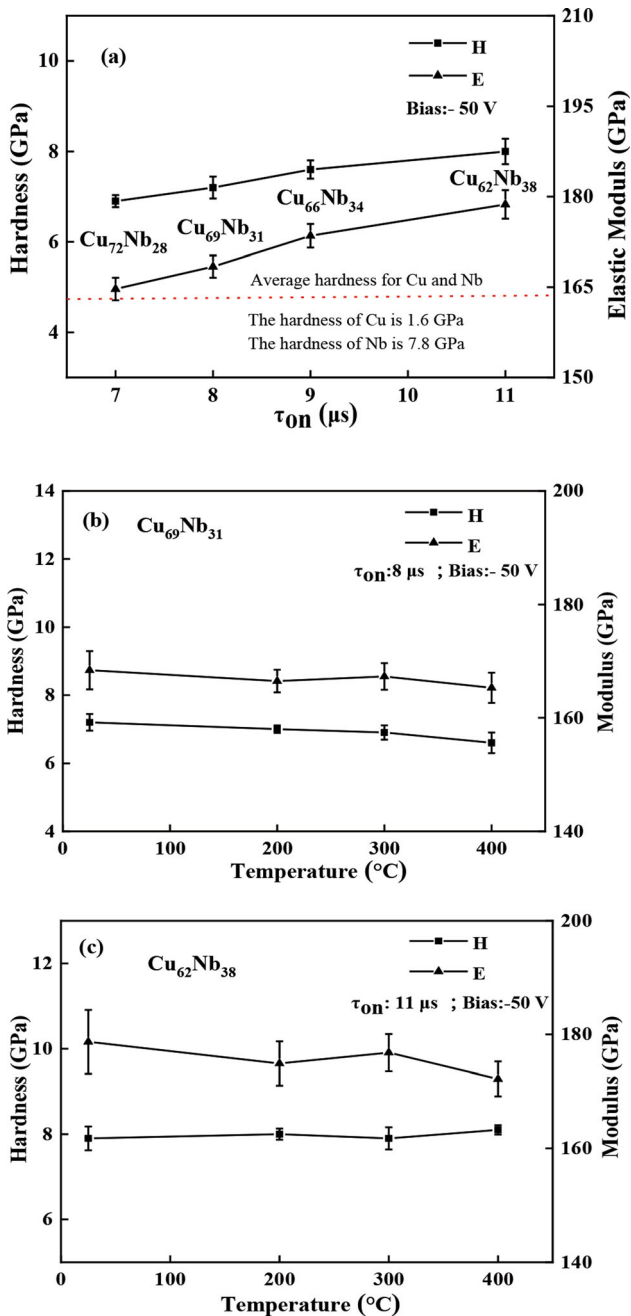
Fig. 5 Hardness and modulus of Cu-Nb films before and after annealing: (a) as-deposited Cu-Nb thin films; (b) $Cu_{69}Nb_{31}$ thin films before and after annealing process; (c) $Cu_{62}Nb_{38}$ thin films before and after annealing process.

Cu-rich phase had a limited role on system hardness, and the grain size of copper and niobium crystals was insensitive to the thermal changes.

Traditionally, high atomic diffusion was not favorable action in alloy design with high thermal stability, and excellent works have focused on suppressing the atomic diffusion (Ref 33). In this work, a thermal insensitive $Cu_{69}Nb_{31}$ thin film with atomic diffusion in a favorable way was co-sputtered by PDCMS and MPPMS with a negative bias of 50 V, and the film showed a typical nanocomposite structure with Cu and Nb nanocrystal embedded into a Cu-rich phase. The self-organized Cu-Nb nanocomposite films should be driven by the depositing flux

arriving the growth front and diffusion behavior in the growth process (Ref 34). Tuning the micropulse on time to a longer time scale, the composition of the Cu-Nb thin films varied from $Cu_{72}Nb_{28}$ to $Cu_{62}Nb_{38}$, and Nb-rich grains gradually segregated owing to the ion bombardments effect.

Cu-Nb binary system is a typical immiscible material with excellent thermal stability, while the mixing enthalpy can turn to be negative in amorphous state by sputtering (Ref 13, 35). The stability of such system prepared by sputtering lies on the competition between the segregation enthalpy ΔH_{seg} and mixing enthalpy ΔH_{mix} (Ref 5). For the main difference among the four Cu-Nb thin films was mainly the grain size of Nb grains, the gain size, distribution and content of Nb in Cu-Nb thin films dominated the thermal stability of the systems as showed in Figs. 1, 3 and 4. After film annealing, the two-step microstructure evolutions were observed which were the precipitation of Nb-rich grains and decomposition of Cu-rich phases showing a typical competition behavior. Note that the current established criterion for designing a thermal stable material relies on the competition between segregation enthalpy ΔH_{seg} and the mixing enthalpy ΔH_{mix}, and the exact relation between ΔH_{seg} and ΔH_{mix} is as follows: $\Delta H_{seg} = \Delta H_{mix} + E_B$ $E_A - (E_{GB} - E_{GB}^A)/x_s^{GB}$, where E_{GB}^A is the enthalpy per atom of a pure solvent grain boundary, E_A and E_B are the enthalpy per atom of the pure solvent and solute, and x_s^{GB} is the fraction of atoms in the grain boundary compound that are solute (Ref 5). It showed that the for a given immiscible alloy with certain composition prepared by sputtering, the thermal stability should mainly determine by the amount of the atoms in the grain boundary influencing by the solute drag effect and pining effect from kinetic and thermodynamic points of view. The results showed that the solute drag effect and pining effect can still work for the constrain of precipitate Cu and Nb grain size in $Cu_{69}Nb_{31}$ thin films as showed in XRD and TEM observations. The anomalous thermal behavior of $Cu_{69}Nb_{31}$ thin films should consider the solute drag effect over the Zener pining since the existence of Cu-riched phase (Ref 19, 36).

4. Conclusion

(1) Cu-Nb thin films were deposited by hybrid modulated pulsed power magnetron sputtering (MPPMS) and pulsed dc magnetron sputtering (dcMS) by varying MPPMS micropulse on time τon from 7 to 11 μs with substrate bias of − 50 V. By increasing the micropulse on time, the content of Cu and Nb in thin films varied from $Cu_{72}Nb_{28}$ to $Cu_{62}Nb_{38}$.

(2) All Cu-Nb thin films showed a typical nanocomposite structure with Cu and Nb nanograins embedded in Cu-riched phases. Before annealing, the as-deposited thin film showed an increase in the precipitate of Nb grains as the increase in the micropulse on time of MPPMS. The precipitate Nb grains showed Nb(110) preferred orientation.

(3) For Cu-Nb thin films before and after annealing, small Nb precipitated particles could be observed, while the grain size of precipitated Nb grain was quite stable with the amount of Nb grains increased after annealing. The redistribution of the element initiated even at a low tem-

perature of 200 °C. The two-step crystallization process endowed the nanocomposite Cu-Nb thin films with a promising potential to be radiation tolerance material.

Conflict of interest

We declare that we have no conflict of interest.

References

1. M.J. Demkowicz, P. Bellon, and B.D. Wirth, Atomic-Scale Design of Radiation Tolerant Nanocomposites, *MRS Bull.*, 2010, **35**(12), p 1–7. https://doi.org/10.1557/mrs2010.704

2. E. Sheu, Y.F. Zhang, H. Kim, D.J. Williams, J.K. Baldwin, and M.J. Demkowicz, Fragmentation of the Edge of a Terminated Cu Nanolayer Within a Nb Matrix Upon Annealing, *Scr. Mater.*, 2023, **225**, p 115168. https://doi.org/10.1016/j.scriptamat.2022.115168

3. M.J. Demkowicz and I.J. Beyerlein, The Effects of Nanoscale Confinement on the Behavior of Metal Laminates, *Scr. Mater.*, 2020, **187**, p 130–136. https://doi.org/10.1016/j.scriptamat.2020.05.057

4. D. Josell, W.C. Carter, and J.E. Bonevich, Stability of Multilayer Structure: Capillary Effect, *Nanostruct. Mater.*, 1999, **12**, p 387–390. https://doi.org/10.1016/S0965-9773(99)00141-5

5. H.A. Murdoch and C.A. Schuh, Stability of Binary of Nanocrystalline Alloys Against Grain Growth and Phase Separation, *Acta Mater.*, 2013, **61**, p 2121–2132. https://doi.org/10.1016/j.actamat.2012.12.033

6. K.O.E. Henrikssona and K. Nordlund, Molecular Dynamics Simulations of Cascades in Strained Carbide Inclusions Embedded in α-Iron, *AIP Adv.*, 2015, **5**, p 117152. https://doi.org/10.1063/1.4936883

7. E.M. Bringa, E. Hall, R.E. Johnson, and R.M. Papalé, Crater Formation by Ion Bombardment as a Function of Incident Angle, *Nucl. Instrum. Methods Phys. Res. Sect. B*, 2002, **193**, p 734–738. https://doi.org/10.1016/S0168-583X(02)00895-9

8. X. Zhou, X.Y. Li, and K. Lu, Enhanced Thermal Stability of Nanograined Metals Below a Critical Grain Size, *Science*, 2018, **360**, p 526–530. https://doi.org/10.1126/science.aar6941

9. K.A. Darling, B.K. VanLeeuwen, C.C. Koch, and R.O. Scattergood, Thermal Stability of Nanocrystalline Fe-Zr Alloys, *Mater. Sci. Eng. A*, 2010, **527**, p 3572–3580. https://doi.org/10.1016/j.msea.2010.02.043

10. T. Chookajorn, H.A. Murdoch, and C.A. Schuh, Design of Stable Nanocrystalline Alloys, *Science*, 2012, **337**, p 951–954. https://doi.org/10.1126/science.1224737

11. K.A. Darling, M. Rajagopalan, M. Komarasamy, M.A. Bhatia, B.C. Hornbuckle, R.S. Mishra, and K.N. Solanki, Extreme Creep Resistance in a Microstructurally Stable Nanocrystalline Alloys, *Nature*, 2016, **537**, p 378–381. https://doi.org/10.1038/nature19313

12. C. Michaelsen, C. Gente, and R. Bormann, The Thermodynamics of Amorphous Phases in Immiscible System: The Example of Sputter-Deposited Nb-Cu Alloys, *J. Appl. Phys.*, 1997, **81**, p 6024–6030. https://doi.org/10.1063/1.364451

13. A. Puthucode, A. Devaraj, S. Nag, S. Bose, P. Ayyub, M.J. Kaufman, and B. Banerjee, De-vitrification of Nanoscale Phase-Separated Amorphous Thin Films in the Immiscible Copper-Niobium System, *Philos. Mag.*, 2014, **94**, p 1622–1641. https://doi.org/10.1080/14786435.2014.892223

14. X. Zhang, N.Q. Vo, P. Bellon, and R.S. Averback, Microstructural Stability of Nanostructured Cu-Nb-W Alloys during High-Temperature Annealing and Irradiation, *Acta Mater.*, 2011, **59**, p 5332–5341. https://doi.org/10.1016/j.actamat.2011.05.009

15. J. Yang, C. Wang, X. Yan, K. Tao, B. Liu, and Y. Fan, Polycrystalline AlN Films of Fine Crystallinity Prepared by Ion-Beam Assisted Deposition, *Appl. Phys. Lett.*, 1993, **62**, p 2790–2791. https://doi.org/10.1063/1.109210

16. A. Anders, A Structure Zone Diagram Including Plasma-Based Deposition and Ion Etching, *Thin Solid Films*, 2010, **518**, p 4087–4090. https://doi.org/10.1016/j.tsf.2009.10.145

17. J. Lin, W.D. Sproul, J.J. Moore, Z. Wu, S. Lee, R. Chistyakov, and B. Abraham, Recent Advances in Modulated Pulsed Power Magnetron Sputtering for Surface Engineering, *JOM*, 2011, **63**(6), p 48–58. https://doi.org/10.1007/s11837-011-0092-4

18. Y.G. Li, Y.L. Lu, Z.T. Jiang, N. Pan, and M.K. Lei, On the Influence of the Micropulse on Nb Thin Films Deposited by MPPMS and DOMS: A Comparative Study, *Surf. Coat. Technol.*, 2020, **421**, p 127464. https://doi.org/10.1016/j.surfcoat.2021.127464

19. M. Kapoor, T. Kaub, K.A. Darling, B.L. Boyce, and G.T. Thompson, An Atom Probe Study on Nb Solute Partitioning and Nanocrystalline Grain Stabilization in Mechanically Alloyed Cu-Nb, *Acta Mater.*, 2017, **126**, p 564–575. https://doi.org/10.1016/j.actamat.2016.12.057

20. R. Banerjee, A. Puthucode, S. Bose, and P. Ayyub, Nanoscale Phase Separation in Amorphous Immiscible Copper-Niobium Alloy Thin Films, *Appl. Phys. Lett.*, 2007, **90**, p 021904. https://doi.org/10.1063/1.2429017

21. G. Greczynski, J. Lu, J. Jensen, I. Petrov, J.E. Greene, S. Bolz, W. Kölker, Ch. Schiffers, O. Lemmer, and L. Hultman, Strain-Free, Single-Phase Metastable $Ti_{0.38}Al_{0.62}N$ Alloys with High Hardness: Metal-Ion ENERGY Versus Momentum Effects during Film Growth by Hybrid High-Power Pulsed/DC Magnetron Cosputtering, *Thin Solid Films*, 2014, **556**, p 87–98. https://doi.org/10.1016/j.tsf.2014.01.017

22. J. Ziegler, J. Biersack, and U. Littmark, *The stopping and range of ions in matter*, Pergamon Press, New York, 1985

23. K.V. Aeken, S. Mahieu, and D. Depla, The Metal Flux From a Rotating Cylindrical Magnetron: a Monte Carlo Simulation, *J. Phys. D-Appl. Phys.*, 2008, **41**, p 205307. https://doi.org/10.1088/0022-3727/41/20/205307

24. T.L. Wang and J.H. Li, Formation of Amorphous Phases in an Immiscible Cu-Nb System Studied by Molecular Dynamics Simulation and Ion Beam Mixing, *Scr. Mater.*, 2007, **57**, p 157–160. https://doi.org/10.1016/j.scriptamat.2007.03.006

25. M. Abboud, A. Motallebzadeh, Ö. Duygulu, R. Maaβ, and S. Özerinç, Microstructure and Nanomechanical Behavior of Sputtered CuNb Thin Films, *Intermetallics*, 2021, **136**, p 107249. https://doi.org/10.1016/j.intermet.2021.107249

26. F. Zeng, B. Zhao, and F. Pan, Metastable Phases Formation in Cu-Nb Films by Ion-Beam-Assisted Deposition, *Nucl. Instrum. Methods Phys. Res. Sect. B*, 2001, **183**, p 311–317. https://doi.org/10.1016/S0168-583X(01)00747-9

27. M. Kateb, H. Hajihoseini, J.T. Gudmundsson, and S. Ingvarsson, Role of Ionization Fraction on the Surface Roughness, Density, and Interface Mixing of the Films Deposited by Thermal Evaporation, DC Magnetron Sputtering, and HiPIMS: An Atomistic Simulation, *J. Vac. Sci. Technol. A*, 2019, **37**, p 031306. https://doi.org/10.1116/1.5094429

28. A.R. Miedema and A.K. Niessen, The Enthalpy of Solution for Solid Binary Alloys of Two 4d-Transition Metal, *Calphad*, 1983, **7**, p 27–36. https://doi.org/10.1016/0364-5916(83)90027-5

29. A.K. Niessen, F.R. de Boer, R. Boom, P.F. de Châtel, W.C.M. Mattens, and A.R. Miedema, Model Predictions for the Enthalpy of Formation of Transition Metal Alloys II, *Calphad*, 1983, **7**, p 51–70. https://doi.org/10.1016/0364-5916(83)90030-5

30. I. Martin-Bragado and A. Rivera, MMonCa: An Object Kinetic Monte Carlo Simulator for Damage Irradiation Evolution and Defect Diffusion, *Comput. Phys. Commun.*, 2013, **184**(12), p 27032710. https://doi.org/10.1016/j.cpc.2013.07.011

31. A. Flink, J.M. Andersson, B. Alling, R. Daniel, J. Sjölén, L. Karlsson, and L. Hultman, Structure and Thermal Stability of Arc Evaporated $(Ti_{0.33}Al_{0.67})_{1-x}Si_xN$ Thin Films, *Thin Solid Films*, 2008, **517**, p 714–721. https://doi.org/10.1016/j.tsf.2008.08.126

32. R.F. Zhang, A.S. Argon, and S. Veprek, Friedel Oscillations are Limiting the Strength of Superhard Nanocomposites and Heterostructures, *Phys. Rev. Lett.*, 2009, **102**, p 015503. https://doi.org/10.1103/PhysRevLett.102.015503

33. W. Xu, B. Zhang, X.Y. Li, and K. Lu, Suppressing Atomic Diffusion with the Schwarz Crystal Structure in Supersaturated Al-Mg Alloys, *Science*, 2021, **373**, p 683–687. https://doi.org/10.1126/science.abh0700

34. V. Elofsson, G.A. Almyras, B. Lü, R.D. Boyd, and K. Sarakinos, Atomic Arrangement in Immiscible Ag-Cu Alloys Synthesized Far-From-Equilibrium, *Acta Mater.*, 2016, **110**, p 114–121. https://doi.org/10.1016/j.actamat.2016.03.023

35. C.G. Ding, J. Xu, D. Shan, B. Guo, and T.G. Langdon, The Thermal Instability Mechanism and Annealed Deformation Behavior of Cu/Nb Nanolaminate Composites, *J. Mater. Sci. Technol.*, 2023, **157**, p 163–173. https://doi.org/10.1016/j.jmst.2023.01.052

36. I. Souli, G.C. Gruber, V.L. Terziyska, J. Zechner, and C. Mitterer, Thermal Stability of Immiscible Sputter-Deposited Cu-Mo Thin Films, *J. Alloy. Compd.*, 2019, **783**, p 208–218. https://doi.org/10.1016/j.jallcom.2018.12.250